Monthly Notices of the ROYAL ASTRONOMICAL SOCIETY

MNRAS **527,** 5117–5130 (2024) https://doi.org/10.1093/mnras/stad3528
Advance Access publication 2023 November 15

Using helium 10 830 Å transits to constrain planetary magnetic fields

Ethan Schreyer [1]★ James E. Owen [1] Jessica J. Spake [2] Zahra Bahroloom[1] and Simone Di Giampasquale[1]

[1]*Astrophysics Group, Department of Physics, Imperial College London, Prince Consort Rd, London SW7 2AZ, UK*
[2]*Division of Geological and Planetary Sciences, California Institute of Technology, Pasadena, CA 91125, USA*

Accepted 2023 November 13. Received 2023 November 6; in original form 2023 February 17

ABSTRACT

Planetary magnetic fields can affect the predicted mass-loss rate for close-in planets that experience large amounts of ultraviolet irradiation. In this work, we present a method to detect the magnetic fields of close-in exoplanets undergoing atmospheric escape using transit spectroscopy at the 10 830 Å line of helium. Motivated by previous work on hydrodynamic and magnetohydrodynamic photoevaporation, we suggest that planets with magnetic fields that are too weak to control the outflow's topology lead to blueshifted transits due to dayside-to-nightside flows. In contrast, strong magnetic fields prevent this day-to-night flow, as the gas is forced to follow the magnetic field's roughly dipolar topology. We post-process existing 2D photoevaporation simulations, computing synthetic transit profiles in helium to test this concept. As expected, we find that hydrodynamically dominated outflows lead to blueshifted transits of the order of the sound speed of the gas. Strong surface magnetic fields lead to unshifted or slightly redshifted transit profiles. High-resolution observations can distinguish between these profiles; however, eccentricity uncertainties generally mean that we cannot conclusively say that velocity shifts are due to the outflow for individual planets. The majority of helium observations are blueshifted, which could be a tentative indication that close-in planets generally have surface dipole magnetic field strengths $\lesssim$0.3 G. More 3D hydrodynamic and magnetohydrodynamic simulations are needed to confirm this conclusion robustly.

Key words: planets and satellites: atmospheres – planets and satellites: magnetic fields.

1 INTRODUCTION

Planets that reside close to their host stars receive significant amounts of high-energy flux. Photoionization of their upper atmospheres results in heating that can drive mass-loss in the form of a hydrodynamic wind (Lammer et al. 2003; Muñoz 2007; Murray-Clay, Chiang & Murray 2009; Owen & Jackson 2012; Kubyshkina et al. 2018). For small, low-mass planets (1–4 $R_\oplus$, $\lesssim$20 $M_\oplus$), photoevaporation can completely strip their primordial hydrogen/helium envelopes, leaving behind a 'stripped core' with a bulk composition similar to Earth's (Lopez & Fortney 2013; Owen & Wu 2013). This photoevaporation-driven evolution has been used to explain the lack of short-period Neptune-sized planets (e.g. Szabó & Kiss 2011; Lundkvist et al. 2016; Owen & Lai 2018), and the bimodal radius distribution of small planets (Fulton et al. 2017; Owen & Wu 2017; Van Eylen et al. 2018; Rogers at al. 2023b). However, other interpretations have been proposed to explain the demographics of close-in, low-mass exoplanets: for example, other mass-loss mechanisms such as core-powered mass-loss (e.g. Ginzburg, Schlichting & Sari 2018; Gupta & Schlichting 2019) or impact-powered mass-loss (e.g. Wyatt, Kral & Sinclair 2020), late-time gas accretion in the formation phase (e.g. Lee & Connors 2021; Lee, Karalis & Thorngren 2022), or separate populations of terrestrial planets and water worlds (e.g. Zeng et al. 2019; Luque & Pallé 2022).

Given this debate, we need to test photoevaporation models using direct observations of atmospheric escape. An unquantified uncertainty when testing these models is the role that magnetic fields play in controlling the outflow and the mass-loss (e.g. Owen & Adams 2019). The photoevaporation models used to match the observed location of the radius valley have not included magnetic fields (e.g. Owen & Wu 2017; Wu 2019; Rogers & Owen 2021; Rogers et al. 2023a, b). Photoevaporative outflows are highly ionized, so they should be influenced by any planetary magnetic fields. The degree to which the planetary magnetic field controls the outflow is determined by the ratio of magnetic pressure to thermal/ram pressure of the outflow (e.g. Adams 2011). If the magnetic pressure dominates near the planetary surface, then the gas is constrained to the topology imposed by the planet's magnetic field. For this 'magnetically controlled' case, analytical and numerical studies have demonstrated that in a region near the equator, the magnetic field lines are closed, and the gas is trapped in a 'dead zone' (e.g. Adams 2011; Trammell, Arras & Li 2011; Owen & Adams 2014; Trammell, Li & Arras 2014; Khodachenko et al. 2015; Matsakos, Uribe & Königl 2015; Arakcheev et al. 2017). Hence, the gas can only escape near the poles, where the gas pressure can open magnetic field lines and

★ E-mail: es2516@ic.ac.uk

© 2023 The Author(s).
Published by Oxford University Press on behalf of Royal Astronomical Society. This is an Open Access article distributed under the terms of the Creative Commons Attribution License (https://creativecommons.org/licenses/by/4.0/), which permits unrestricted reuse, distribution, and reproduction in any medium, provided the original work is properly cited

Downloaded from https://academic.oup.com/mnras/article/527/3/5117/7424142 by Imperial College London Library user on 31 January 2024

drive a transonic wind. Alternatively, if the thermal/ram pressure dominates everywhere, the gas will open all field lines (dragging the magnetic field with it). In this 'hydrodynamic case', the outflow should represent those seen in purely hydrodynamic (HD) simulations (e.g. Stone & Proga 2009; Owen & Adams 2014; Khodachenko et al. 2015; Tripathi et al. 2015; Carroll-Nellenback et al. 2016; McCann et al. 2019; Debrecht et al. 2020; Carolan et al. 2021a).

In the magnetically controlled case, only a fraction of the planetary surface supports open field lines, and the mass-loss rate is suppressed compared to the hydrodynamic case. 2D magnetohydrodynamic (MHD) simulations have suggested that surface magnetic field strengths as low as ∼0.3–3 G can suppress the mass-loss rate of hot Jupiters by an order of magnitude (Owen & Adams 2014; Trammell et al. 2014; Khodachenko et al. 2015). The critical magnetic field strengths required to suppress mass-loss rates are smaller or comparable to many of the planetary magnetic field strengths in our Solar system (e.g. Jupiter's dipole moment is ∼4 G; Stevenson 2003; Connerney et al. 2022). Therefore, it is important to consider the effects of magnetic fields on escape for exoplanets and understand how to determine their impact observationally. 3D MHD simulations that include the stellar wind also found that the planetary mass-loss rate decreases with planetary magnetic field strength (Khodachenko et al. 2021). However, we note that similar simulations run by Carolan et al. (2021b) show the opposite dependence, and the differences are yet to be fully understood.

For lower mass planets, strong planetary magnetic fields that suppress mass-loss could significantly affect their evolution. Owen & Adams (2019) studied the effect that magnetic fields would have on the location of the radius valley. If these planets had surface magnetic field strengths $\gtrsim$3 G at the age of a few hundred Myr,[1] then their cores would need to be ice rich in order to match the observed radius valley. However, since the planets below the radius gap (that have well-constrained masses) generally have densities consistent with an Earth-like composition (Dressing et al. 2015; Dorn et al. 2018; Van Eylen et al. 2019), they argue that this implies that the low-mass, close-in exoplanet population does not possess strong magnetic fields. Specifically, Owen & Adams (2019) argued that the dynamo-generated fields in the hydrogen/helium envelopes of mini-Neptunes must be weak ($B \lesssim 0.3$ G) at young ages.

Unlike small planets, hot Jupiters are thought to be stable to atmospheric mass-loss independent of whether or not magnetic fields suppress escape (e.g. Hubbard et al. 2007; Owen & Wu 2013; Jin et al. 2014). However, the strength of their magnetic fields is still of much interest. Hot Jupiters have radii larger than expected from interior structure models (Laughlin, Crismani & Adams 2011; Thorngren & Fortney 2018). In order to explain this discrepancy, these planets require an extra source of energy that must be deposited into the interior (e.g. Bodenheimer, Lin & Mardling 2001; Guillot & Showman 2002; Arras & Socrates 2010; Batygin & Stevenson 2010; Youdin & Mitchell 2010; Komacek & Youdin 2017). One popular explanation for this extra energy is Ohmic dissipation, in which the interaction of zonal winds and the planetary magnetic field generates electrical currents that resistively heat the interior (Batygin & Stevenson 2010; Perna, Menou & Rauscher 2010; Batygin, Stevenson & Bodenheimer 2011; Menou 2012; Rauscher & Menou 2013; Ginzburg & Sari 2016). Current modelling suggests that explaining the hot Jupiter radius anomaly in this way requires hot Jupiters to possess sizeable magnetic fields. For example, using 3D MHD simulations of the atmosphere of HD 209458b, Rauscher & Menou (2013) argue that the magnetic field must be greater than 3–10 G for Ohmic dissipation to be responsible for its inflated radius. For a few hot Jupiters hosting stars, Cauley et al. (2019) found tentative evidence of magnetic star–planet interactions. From variations in the Ca II K line, they inferred these planets to have large magnetic fields ∼20–100 G. However, we note that Cauley et al. (2019) caution that the detected variability may be unrelated to the presence of a planet, and hence does not constrain planetary magnetic fields. Independently, using a scaling law relating the magnetic energy density to the density and intrinsic luminosity of bodies ranging from Earth to low-mass stars, Christensen, Holzwarth & Reiners (2009) estimated the magnetic field of hot Jupiters to have magnetic field strengths of the order of 20–50 G. In contrast, Grießmeier et al. (2004) argued that tidally locked hot Jupiters should have a much smaller magnetic field than Jupiter due to their slow rotation rate.

To determine whether the effects of magnetic fields need to be accounted for in evolutionary modelling, we need to compare theoretical predictions of 'magnetically controlled' and 'hydrodynamic' outflows to direct observations of atmospheric escape. Additionally, these observations can be used to put constraints on the magnetic field strength of planets. The two most commonly used lines to directly observe atmospheric escape are Lyman-α (e.g. Vidal-Madjar et al. 2003; Lecavelier Des Etangs et al. 2010; Kulow et al. 2014) and He I 10 830 Å (e.g. Allart et al. 2018; Nortmann et al. 2018; Spake et al. 2018), which originates from the metastable 2^3S state of helium.

Kislyakova et al. (2014) and Ben-Jaffel et al. (2022) inferred the magnetic field properties of HD 209458b and HAT-P-11b, respectively, by matching the transit spectrum deduced from 3D outflow models to Lyman-α transits. In general, this approach is challenging because absorption in the interstellar medium generally obscures the line core (e.g. Landsman & Simon 1993), and therefore Lyman-α transits probe material at high radial velocities and distances far from the planet $\gtrsim 10 R_p$ where the outflow is affected by the circumstellar environment (e.g. Owen et al. 2023). This causes observations to be degenerate with properties of the circumstellar environment, making it difficult to link observations to fundamental planetary quantities, such as the planetary magnetic field strength.

The helium line may provide a better tool in this endeavour. It probes material closer to the planet (e.g. MacLeod & Oklopčić 2022) and observations can be done at high spectral resolution ($R \gtrsim$ 30 000) since it is accessible from the ground. This provides a unique opportunity to study the kinematics of the outflow near the planet. Oklopčić et al. (2020) proposed using spectropolarimetry of this line to detect magnetic fields; however, this method is not currently feasible with 10 m class telescopes but may be possible in the future with 30 m class telescopes.

Here, we propose a method for detecting the presence of magnetic fields strong enough to control the topology of the outflow using transmission spectroscopy in the 10 830 Å line of helium. Motivated by previous HD and MHD simulations, we suggest that 'hydrodynamic' outflows (i.e. outflows where the planetary magnetic fields are dynamically unimportant) should lead to blueshifted transmission spectra due to gas flowing from the hot dayside to the cold nightside (towards the observer during transit) as a result of pressure gradients from the anisotropic heating. In contrast, strong magnetic fields prevent the day-to-night outflow and cause the gas to move away from the observer during transit. As a result, we suggest that

[1] Since this is when the host stars are bright in the XUV, and thus when most of the mass-loss occurs (e.g. Jackson, Davis & Wheatley 2012).

Downloaded from https://academic.oup.com/mnras/article/527/3/5117/7424142 by Imperial College London Library user on 31 January 2024

'magnetically controlled' outflows will produce transmission spectra that are (weakly) redshifted.

2 THE EFFECT OF MAGNETIC FIELDS ON PHOTOEVAPORATION

In general, the planetary outflow is sensitive to both planet properties and the stellar environment. Following Owen & Adams (2014), one can coarsely partition the outflow into regimes based on the relative strength of the stellar magnetic field, stellar wind ram pressure, planetary magnetic field, and planetary wind ram pressure. In this work, we consider regimes where either the ram pressure of the planetary wind or the planetary magnetic field pressure dominates the stellar components close to the planetary surface, where most of the helium absorption occurs. We can estimate whether the outflow is magnetically controlled by considering the dimensionless quantity Λ, which is the ratio of the ram pressure of the wind to the magnetic pressure of the planet. For a planet with a dipolar magnetic field, this ratio is equal to

$$\Lambda_{\rm p} = \frac{2\dot{M}vr^4}{B_0^2 R_{\rm P}^6}, \tag{1}$$

where $\dot{M}$ is the outflow rate, B_0 is the surface magnetic field strength of the body, $R_{\rm P}$ is the radius of the body, and r is the distance to the centre of the body. When $\Lambda_{\rm p} \ll 1$, the flow is magnetically controlled, and the outflowing gas is forced to follow magnetic field lines. When $\Lambda_{\rm p} \gg 1$, the outflow will drag magnetic field lines and should follow a flow structure similar to a pure hydrodynamic outflow. Using an 'energy-limited' outflow (e.g. Baraffe et al. 2004), where

$$\dot{M} = \eta \frac{\pi F_{\rm XUV} R_{\rm P}^3}{4GM}, \tag{2}$$

we estimate the threshold magnetic field such that magnetic pressure and ram pressure are equal (i.e. $\Lambda_{\rm p} = 1$). For fiducial parameters appropriate for a typical hot Jupiter, this is

$$B \approx 0.015 \left(\frac{\eta}{0.1}\right)^{\frac{1}{2}} \left(\frac{F_{\rm XUV}}{10^4\ {\rm erg\ s^{-1}}}\right)^{\frac{1}{2}} \left(\frac{v}{10\ {\rm km\ s^{-1}}}\right)^{\frac{1}{2}} \left(\frac{M_{\rm p}}{M_{\rm J}}\right)^{-\frac{1}{2}} \times \left(\frac{R_{\rm p}}{R_{\rm J}}\right)^{\frac{1}{2}} \left(\frac{r}{R_{\rm p}}\right)^{2} {\rm G}. \tag{3}$$

2.1 Post-processing existing simulations

To assess whether 'hydrodynamic' and 'magnetically controlled' outflows will produce blueshifted and redshifted transit spectra, respectively, we want to compare the synthetic transit spectra produced from simulations. There are no 3D radiation-hydrodynamic photoevaporation simulations that include helium and magnetic fields. Given the complexity of post-processing simulations (as detailed in Section 2.2), which would be difficult in 3D, as a first step, we choose to use existing 2D photoevaporation simulations of a hot Jupiter presented in Owen & Adams (2014). These radiation-hydrodynamic simulations did and did not include magnetic fields for the same set-up and are ideal for our experiment. To analyse the case where the ram pressure of the planetary outflow dominates over the magnetic field of the planet ($\Lambda_{\rm p} > 1$), we use a purely hydrodynamic simulation of the outflow. In the opposite case, where magnetic pressure dominates over ram pressure of the planetary outflow ($\Lambda_{\rm p} < 1$), we use MHD simulations of the outflow.

In these simulations, the planet has a dipolar magnetic field. The planetary dipole was chosen to be parallel to the orbital angular momentum vector of the planet. There are currently no constraints on the geometry of the magnetic field of exoplanets. However, since these planets are very close to their host stars, they are often assumed to be tidally locked. Thus, as a starting point, it is sensible to guess that any dynamo-generated magnetic field may be similar to Jupiter's or Saturn's and (almost) points along the rotation axis.

In some of the simulations, an additional component corresponding to the stellar magnetic field was added. This contribution is modelled as a constant field that points along the pole of the planet:

$$B_* = \beta_* B_{\rm p} \hat{z}, \tag{4}$$

where β_* controls the relative strength of the stellar and planetary magnetic fields.

The original simulations were performed on a spherical polar grid (r, θ), which we can convert to Cartesian coordinates (x, z), where the x-axis points along the line joining the star and the planet and the z-axis is parallel to the planet's orbital angular momentum axis. It is important to state that atmospheric escape is generally a 3D process, and therefore several assumptions need to be made in order to be able to perform sensible 2D simulations. First, the planet needs to be tidally locked to have a constant dayside and nightside. At the same time, rotational effects are ignored. Inside the Hill sphere, these effects are small (Murray-Clay et al. 2009) and can be ignored; however, they are important for shaping the flow on the largest scales (e.g. McCann et al. 2019). Since absorption by helium generally comes from close to the planet, this approximation is reasonable.

In the hydrodynamic case, these approximations mean that the outflow is rotationally symmetric around the line joining the planet to the sub-stellar point. The presence of this magnetic field stops this set-up from being rotationally invariant, such that the flow is no longer globally axisymmetric. Therefore, the simulations required each cell to locally have the property that $\partial_\phi = 0$. Since the magnetic field suppresses the azimuthal flow, this approximation is realistic. Thus, the simulation can be considered a thin slice of the domain in the x-z plane. Since the magnetic field predominately governs the outflow geometry, we expect the flow structure on the dayside to be similar as we rotate around the dipole axis. On the nightside, the outflow is suppressed since heat is not efficiently transported across magnetic field lines. As a result, only the dayside of the atmosphere was simulated [see section 5.1 of Owen & Adams (2014) or Trammell et al. (2014)].

2.2 Addition of helium

The lifetime of the metastable triplet level in the outflow is determined by the rates of collisional, radiative, and photoionization processes that depopulate it. As radiative transitions into the ground state are highly suppressed (Drake 1971), depopulation of this state is dominated by transitions due to collisions and photoionization (e.g. Oklopčić & Hirata 2018; Oklopčić 2019). In the outflow, the lifetime of the metastable state may be comparable to the flow time-scale (see fig. 4 of Oklopčić 2019). Thus, the helium metastable level is often *not* in local statistical equilibrium. This means traditional post-processing techniques of simply using the gas' local properties to compute absorption cross-sections are inappropriate. Therefore, we must compute the level populations by solving the time-dependent radiative transfer equations for gas parcels moving in the outflow.

We assume that the gas is composed of solar abundances of hydrogen and helium; however, we note that the mass fraction of helium in the outflow can be adjusted depending on how efficiently helium is expected to be dragged in the predominantly hydrogen flow (e.g. Malsky & Rogers 2020). Helium is not expected to contribute

Downloaded from https://academic.oup.com/mnras/article/527/3/5117/7424142 by Imperial College London Library user on 31 January 2024

to the cooling of the gas, and therefore the predominant way that it affects the outflow is by raising its mean molecular weight. For a solar abundance of helium, the sound speed of the gas can be modified ∼25 per cent. Ultimately, though, adding helium should not have a large effect on the geometry of the outflow. Therefore, it is reasonable to consider the pure flow structure of the pure hydrogen outflow simulated by Owen & Adams (2014) as representative of a hydrogen–helium outflow. Similarly, the distribution of helium ions and atoms in each electronic state has little impact on the outflow structure.

3 METHODS

3.1 Helium distribution in the outflow

The first task is to calculate the distribution of helium atoms in the outflow. We track the fraction of helium in the neutral singlet and triplet states along streamlines in the outflow. We only track the number of neutral helium atoms in the ground state 1^1S and metastable 2^3S state since excited states quickly radiatively decay to one of these two states with a matching singlet/triplet configuration. Our problem has two parts: (i) determining streamlines in the flow and (ii) calculating the fraction of helium in the triplet state along these streamlines.

In the case of the pure hydrodynamic flow, we solve for the 2D position of a streamline as a function of length, l, down the streamline using equations

$$\frac{\mathrm{d}r}{\mathrm{d}l} = \frac{u_r}{u}, \tag{5}$$

$$\frac{\mathrm{d}\theta}{\mathrm{d}l} = \frac{u_\theta}{ru}. \tag{6}$$

We then derive the steady state distribution of helium atoms along streamlines using equations (7) and (8), which account for the major transitions in and out of the singlet and triplet states of helium (Oklopčić & Hirata 2018):

$$\begin{aligned} u\frac{\mathrm{d}f_1}{\mathrm{d}l} &= (1 - f_1 - f_3)n_\mathrm{e}\alpha_1 + f_3A_{31} + f_3q_{31a}n_\mathrm{e} \\ &\quad + f_3q_{31b}n_\mathrm{e} + f_3Q_{31}n_\mathrm{HI} - f_1\phi_1e^{-\tau_1} - f_1q_{13}n_\mathrm{e}, \end{aligned} \tag{7}$$

$$\begin{aligned} u\frac{\mathrm{d}f_3}{\mathrm{d}l} &= (1 - f_1 - f_3)n_\mathrm{e}\alpha_3 - f_3A_{31} - f_3q_{31a}n_\mathrm{e} \\ &\quad - f_3q_{31b}n_\mathrm{e} - f_3Q_{31}n_\mathrm{HI} - f_3\phi_3e^{-\tau_3} + f_1q_{13}n_\mathrm{e}. \end{aligned} \tag{8}$$

f_1 and f_3 are neutral helium's singlet and triplet fractions, respectively. n_e and n_HI are the number density of electrons and hydrogen atoms, respectively. ϕ_1 and ϕ_3 are the photoionization rates for the singlet and triplet states, respectively. We calculate the photoionization rate for the singlet and triplet states by assuming that all the photoionizing flux is concentrated at a photon energy $\overline{h\nu}$ of 24.6 and 4.8 eV, respectively.

$$\phi_1 = \int_{24.6\,\mathrm{eV}}^{\infty} \frac{F_\nu}{h\nu}\sigma_1(\nu)\mathrm{d}\nu \approx \frac{F_{\overline{\nu}}}{h\nu}\sigma_1(\overline{\nu}), \tag{9}$$

$$\phi_3 = \int_{4.8\,\mathrm{eV}}^{13.6\,\mathrm{eV}} \frac{F_\nu}{h\nu}\sigma_3(\nu)\mathrm{d}\nu \approx \frac{F_{\overline{\nu}}}{h\nu}\sigma_3(\overline{\nu}). \tag{10}$$

Based on the spectral energy distribution for late K stars from the MUSCLES survey (France et al. 2016; Loyd et al. 2016; Youngblood et al. 2016), we estimate the total singlet ionizing flux to be 0.2 of the hydrogen ionizing flux and the total triplet ionizing flux to be about the same hydrogen ionizing flux. As the simulations were run at high ultraviolet (UV) fluxes ∼10^6 erg cm^{-2} s^{-1}, we set $F_{\overline{\nu}} = 2 \times 10^5$ and 10^6 erg cm^{-2} s^{-1} for the singlet and triplet states, respectively. We varied these fluxes by an order of magnitude in both directions and found that it did not qualitatively affect our results. σ_i is the photoionization cross-section of the state. The photoionization cross-sections for these photons are 5.48×10^{-18} cm^2 (Hummer & Storey 1998) and 7.82×10^{-18} cm^2 (Brown 1971), respectively. In this work, we set both $\tau_1 = 0$ and $\tau_3 = 0$. Since hydrogen also absorbs 24.4 eV radiation, we expect the $\tau = 1$ surface to 24.4 eV photons to be above the $\tau = 1$ surface to 4.8 eV photons (and close to the hydrogen ionization front in the simulation). Since the main pathway to populate the triplet state is by photoionization of the singlet state and then recombination into the triplet state, we expect that this will underestimate the triplet fraction below the $\tau = 1$ surface to 24.4 eV. However, since the hydrogen ionization front is deep in the atmosphere of the planet (in these simulations, it is $\sim 1.03R_\mathrm{p}$), the gas below this surface contributes minimally to the overall transit signal.

The recombination and collisional excitation/de-excitation coefficients depend on the temperature of the gas. As the simulations were run for high UV fluxes ($\gtrsim 10^6$ erg cm^{-2} s^{-1}), the gas is in the radiative-recombination regime (Murray-Clay et al. 2009) and therefore thermostats to ∼10^4 K above the ionization front. As a result, we use all coefficients at 10^4 K. $\alpha_1 = 2.16 \times 10^{-13}$ cm^3 s^{-1} and $\alpha_3 = 2.25 \times 10^{-13}$ cm^3 s^{-1} are the case A recombination coefficients for the singlet and triplet states, respectively (Osterbrock & Ferland 2006). The electron density (n_e) is calculated in the Owen & Adams (2014) simulations, which only accounted for electrons produced by the ionization of hydrogen atoms since this is the dominant source. $A_{31} = 1.272 \times 10^{-4}$ s^{-1} is the radiative transition rate between the metastable triplet state and the ground singlet state (Drake 1971). The transitions between the triplet and singlet states due to collisions with electrons are denoted by the temperature-dependent coefficients:

$$q_{ij} = 2.1 \times 10^{-8}\sqrt{\frac{13.6\,\mathrm{eV}}{kT}}\exp\left(-\frac{E_{ij}}{kT}\right)\frac{\Upsilon_{ij}}{w_i}\ \mathrm{cm}^3\ \mathrm{s}^{-1}, \tag{11}$$

where E_{ij} is the energy difference between the states from Martin (1973), w_i is the statistical weight of the state, and Υ_{ij} is the effective collision strength from Bray et al. (2000). At 10^4 K, the two transitions from the metastable state to singlet levels are given by $q_{31a} = 2.7 \times 10^{-8}$ cm^3 s^{-1} and $q_{31b} = 5.2 \times 10^{-9}$ cm^3 s^{-1}. The transition from the ground singlet state to the metastable state is given by $q_{13} = 5.7 \times 10^{-19}$ cm^3 s^{-1}. Finally, transitions out of the metastable state due to collisions with hydrogen atoms via associative ionization and Penning ionization have a combined rate of $Q_{31} \sim 5 \times 10^{-10}$ cm^3 s^{-1} (Roberge & Dalgarno 1982). Equations (5), (6), (7), and (8) form a set of coupled first-order differential equations. The streamlines are initialized at a constant radius $1.02R_\mathrm{p}$ with an initial singlet and triplet fraction that is in equilibrium at 500 K with $\phi_1 = \phi_3 = 0$. We solve these differential equations numerically using the implementation of the LSODA method (Petzold 1983) provided in the SCIPY library (Virtanen et al. 2020). For numerical stability, we solve equations (7) and (8) as function of $\log(l)$. The absolute and relative tolerances used are 1×10^{-13} and 1×10^{-10}, respectively, and the maximum step size chosen is 1×10^{-3}. All gas properties required to solve these equations (e.g. density, velocity, etc.) were interpolated from the original simulations using bivariate spline interpolation over the polar grid. To calculate the metastable helium fraction at any point in the outflow, we interpolate the values for 50 streamlines, linearly spaced in angle, originating on the planet's dayside. Testing indicates that this is sufficient to calculate

Downloaded from https://academic.oup.com/mnras/article/527/3/5117/7424142 by Imperial College London Library user on 31 January 2024

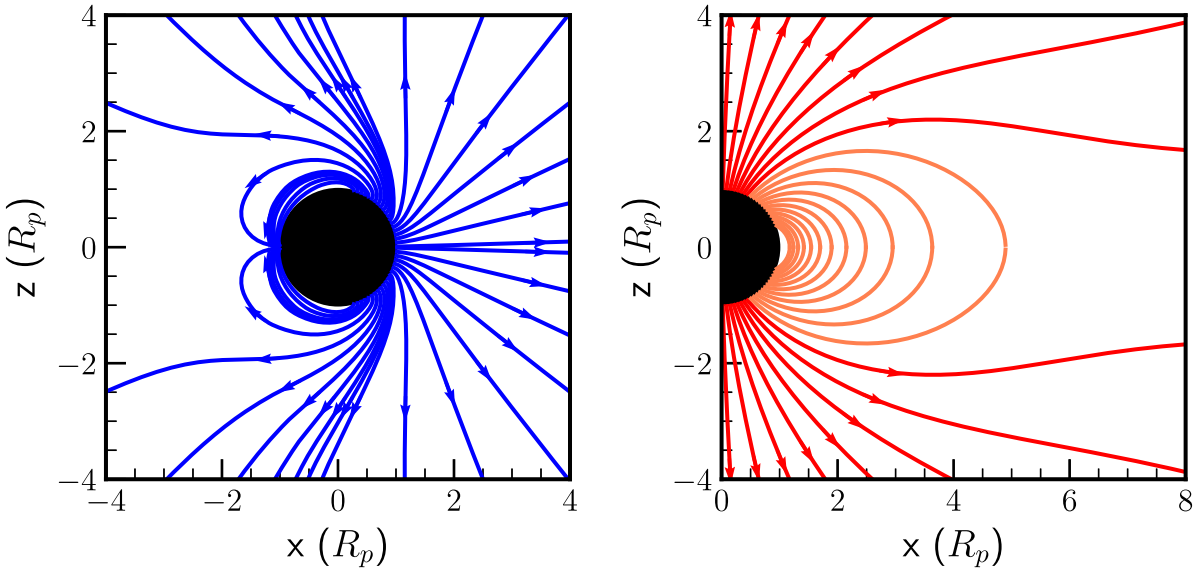


Figure 1. Left: Streamlines of the outflow for the case of a planet without a magnetic field. The star is located to the right of the planet along the line $z = 0$. The planet is shown by a black circle centred on the origin. The orientation is the same for all subsequent 2D plots. Due to anisotropic heating, the dayside is much hotter than the nightside. The resulting pressure gradients cause the outflow to wrap around the planet, creating gas travelling towards an observer in transit in the transmission region. Right: Magnetic field lines for a planet with a surface magnetic field strength of 3 G. The magnetic field lines are closed (shown in orange) where the magnetic field is strong enough to confine the flow. The open magnetic field lines (shown in red), where the magnetic field cannot confine the outflow, coincide with gas streamlines. The direction of the arrows shows the direction of the outflow. In this case, the magnetic field prevents the dayside-to-nightside outflow and causes the gas to move away from the observer in transit in the transmission region.

the transmission spectrum accurately. Fig. 1 shows how streamlines originating on the planet's dayside wrap around to the nightside.

In the MHD case, we have to consider both the field centred on the poles where the magnetic field lines are opened by the outflow and a region centred on the equator where magnetic pressure dominates over thermal pressure so that the field lines are closed. Since the fluid is required to follow magnetic field lines (and magnetic field lines are dragged along by the fluid), we can determine the streamlines of our gas in the open region by tracing magnetic field lines. This is helpful because we can simultaneously determine the region in which the field lines are closed. These are calculated analogously to equations (5) and (6) replacing velocity with magnetic field:

$$\frac{\mathrm{d}r}{\mathrm{d}l} = \frac{B_r}{B}, \tag{12}$$

$$\frac{\mathrm{d}\theta}{\mathrm{d}l} = \frac{B_\theta}{rB}, \tag{13}$$

where B_r and B_θ are the radial and angular components of the magnetic field, respectively. Fig. 1 shows the magnetic field lines for a fiducial planetary magnetic field strength of 3 G. We use this value of the planetary magnetic field to illustrate the magnetically controlled case throughout the rest of the paper.

In the regions where the streamlines are open, we solve the steady state distribution of helium atoms using equations (7) and (8) as in the hydrodynamic case. In the regions in which they are closed, the gas is approximately in magnetohydrostatic equilibrium, and as a result, the helium-level populations are in statistical equilibrium. Therefore, we solve for the distribution of helium atoms using equations (7) and (8) by setting the advection term (the left-hand side) to zero. The method used to solve these equations numerically is the same as the hydrodynamic one, with the addition of a step to check whether the field line is open or closed to decide to solve the non-equilibrium or equilibrium equation for the distribution of helium atoms.

In Fig. 2, we show the number density profiles of helium in the triplet state for the hydrodynamic and magnetically controlled outflow.

3.2 Computing synthetic transit profiles

Our goal is to calculate the absorption of stellar radiation at 10 830 Å due to the presence of the escaping helium. To elucidate the basic principles, we produce synthetic transmission spectra at mid-transit for the planet transiting with an impact parameter of zero. Since the simulations used to generate the densities and velocities of the outflow are 2D, it is only at mid-transit and with an impact parameter of zero that our approximate symmetry is applicable.

With the assumptions described in Section 2.1, the outflow in the purely hydrodynamic case is rotationally invariant around the line connecting the star and planet (x-axis). This symmetry means that we can identify the z coordinate of our grid with the radial coordinate on the stellar disc. Therefore, the optical depth of the outflow for a ray emanating at any point on the stellar disc is only a function of z and is given by equation (14). This can be integrated over the stellar disc to give the excess absorption caused by the escaping gas:

$$\tau_\nu(z) = \int_{-\infty}^{\infty} n_3(x, z)\sigma_\nu(u_x, T)\mathrm{d}x, \tag{14}$$

$$\text{Excess Depth}(\nu) = \frac{2\int_{R_\mathrm{p}}^{R_\mathrm{s}} e^{-\tau_\nu(z)} z\mathrm{d}z + R_\mathrm{p}^2}{R_\mathrm{s}^2}, \tag{15}$$

where n_3 is the number density of helium atoms in the metastable state, R_p and R_s are the radius of the planet and star, respectively, and σ_ν is the absorption cross-section of the helium to photons at a frequency ν, which is a function of the line-of-sight velocity of the gas, u_x, and the temperature. The absorption cross-section is given by

$$\sigma_\nu = \frac{\pi e^2}{m_\mathrm{e} c} f \Phi(u_x, T), \tag{16}$$

Downloaded from https://academic.oup.com/mnras/article/527/3/5117/7424142 by Imperial College London Library user on 31 January 2024

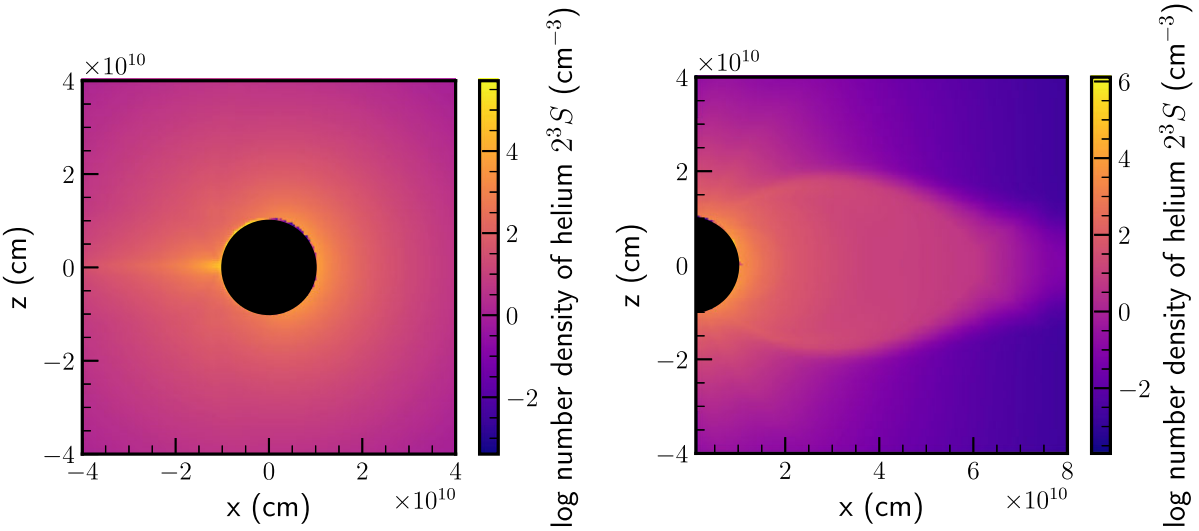


Figure 2. The number density of helium in the 2^3S state in the outflow for the hydrodynamic case (left) and the magnetically controlled case (right). In the hydrodynamic case, the density appears to be fairly spherically symmetric. In the magnetically controlled case, the region with closed magnetic field lines has a higher number density of metastable helium atoms than the outflowing regions. This is primarily because the total number density of gas in this region is higher, as it is in hydrostatic equilibrium.

where e and m_e are the charge and mass of the electron, respectively, c is the speed of light, f is the oscillator strength of the transition, and Φ is the Voigt line profile. The Gaussian part of the Voigt profile has a standard deviation of σ; the Lorentzian part has a half-width at half-maximum of γ, and the line centre has been Doppler shifted to ν.

$$\sigma = \sqrt{\frac{k_b T}{m_{\rm He} c^2}}\nu_0, \quad \gamma = \frac{A}{4\pi}, \quad \nu = \nu_0\left(1 - \frac{u_x}{c}\right). \tag{17}$$

Here, ν_0 is the rest frequency of the helium line, and $A = 1.022 \times 10^7$ s^{-1} is the Einstein A coefficient taken from the NIST atomic data base (Kramida et al. 2022). It is worth noting that the $2^3\text{S} \rightarrow 2^3\text{P}$ transition in Helium actually consists of three distinct lines at 10 830.34, 10 830.25, and 10 829.09 Å due to fine structure splitting. The first two of these transitions are blended; however, the third can be distinguished at the spectral resolution of current instruments. The oscillator strength for these transitions, taken from the NIST atomic data base (Kramida et al. 2022), are given by 0.300, 0.180, and 0.060, respectively. The absorption cross-section at any wavelength is calculated by summing up the contribution from these three transitions.

Similar to Oklopčić & Hirata (2018), when computing the optical depth, we only took into account gas within the Hill sphere of the planet, which we choose to have a radius of $4R_p$. This approximately corresponds to the Hill sphere radius of a Jupiter-mass planet around a solar-mass star at 0.04 au. Beyond the Hill sphere, the outflow is significantly affected by the Coriolis force, the stellar tidal field, and the stellar wind. Here, the model is no longer applicable. However, unless the stellar wind is very strong, these regions do not contribute greatly at mid-transit (e.g. MacLeod & Oklopčić 2022). If the planet is further away from the star or the magnetic field is strong, the planetary outflow may not be affected by the circumstellar environment at larger distances from the planet. In Appendix A, we provide transit spectra taking into account gas up to $8R_p$ to illustrate this effect.

To do this calculation, we construct a linearly spaced 300×600 cell grid in the (x, z) plane, with x in the range $[-4R_p, 4R_p]$ and z in the range $[R_p, 4R_p]$. The integrals in equations (14) and (15) are computed with this grid using a middle Riemann sum.

The method we use in the magnetic case is different. As discussed above, the rotational symmetry around the line connecting the star and planet (x-axis) present in the purely hydrodynamic case is broken by the dipolar structure of the magnetic field. Therefore, we cannot simply compute the 3D density structure by rotating the 2D density distribution around the x-axis. The presence of a planetary magnetic field shuts off the outflow on the nightside planet since heat cannot be transported effectively across magnetic field lines. Therefore, we set the density of helium on the nightside of the planet to zero. On the dayside, we build the 3D density distribution by rotating the 2D density of helium distribution around the z-axis (symmetry axis of the dipole). In order to account for the reduction of UV flux incident on the atmosphere away from the substellar line due to geometrical effects, we scale the number density of helium in the triplet state in each 2D slice by the square root of the reduction of incident UV flux at the base of the slice. We do this because the simulations are done at high UV fluxes such that the outflow is in ionization–recombination equilibrium. In this regime, the temperature of the outflow thermostats to 10^4 K and the density at the base of the outflow is proportional to the square root of the incident UV flux (e.g. Murray-Clay et al. 2009; Owen & Alvarez 2016).

To perform synthetic observations, we create a 3D cylindrical grid from the Cartesian product of a 2D grid on the stellar disc and a 1D grid along the line connecting the star and planet. The 1D grid has 150 cells and ranges from $[0, 4R_p]$. The 2D grid on the stellar disc has 400 cells. We calculate the optical depth of the outflow at the centre of each cell on the stellar disc by integrating through the 3D density distribution using a middle Riemann sum. This can then be translated into an excess depth by integrating over the stellar disc using a double Riemann sum:

$$\text{Excess Depth}(\nu) = \frac{\sum_j e^{-\tau_{\nu,j}} A_j + \pi R_p^2}{\pi R_s^2}, \tag{18}$$

Downloaded from https://academic.oup.com/mnras/article/527/3/5117/7424142 by Imperial College London Library user on 31 January 2024

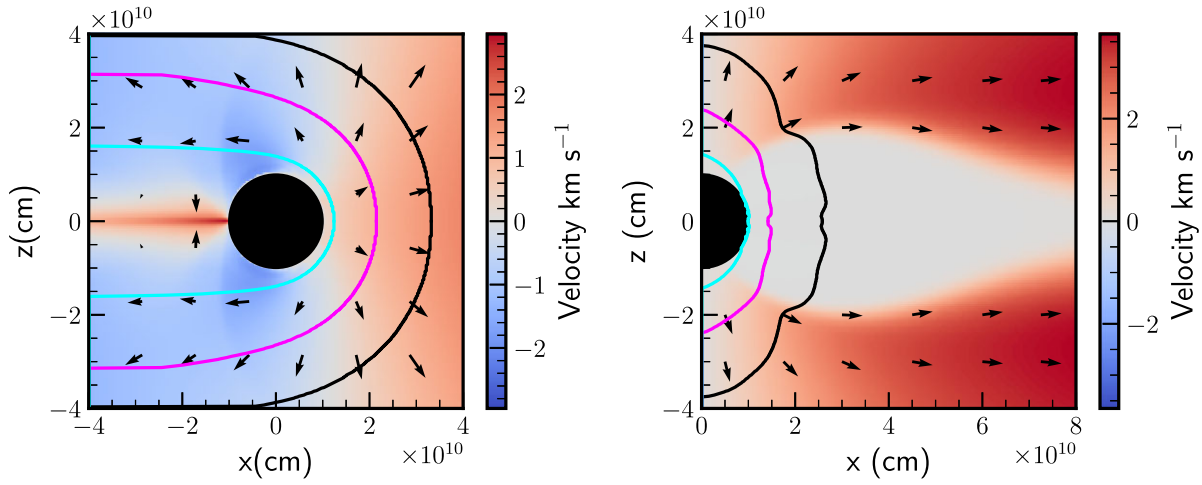


Figure 3. Colour map of the line-of-sight velocity of the outflowing gas in the hydrodynamic case (left) and the magnetically controlled case (right). Contours mark the line-of-sight optical depth integrated over a 2 Å bin around the peak absorption wavelength. From out-to-in, these mark the $\tau = 0.01, 0.1,$ and 1 surfaces (shown in black, magenta, and cyan respectively). The arrows show the velocity field.

where A_j is the area of the jth cell. Fig. 3 shows the line of sight velocity of the gas for an observer whilst the planet is at mid-transit. Contours mark the line of sight optical depth integrated over a 2 Å bin around the peak absorption wavelength.

4 RESULTS

Fig. 4 shows the excess transit depth for the hydrodynamic and magnetically controlled outflows. As expected, we find that the hydrodynamic outflow leads to a blueshifted spectrum. Fig. 3 shows that most of the absorption comes from the terminator, where gas is moving towards the observer in transit. The peak absorption is at -8.3 km s^{-1}, which is of the order of the sound speed of the outflowing gas. It is worth noting that we still see significant absorption in the red wing due to absorption from gas moving towards the star (away from the observer in transit), which has originated from low latitudes on the planet. As a result, the spectrum is asymmetric and broader than expected from thermal broadening.

In contrast, a planet with a 3 G magnetic field shows a symmetric transit spectrum, with a peak absorption centred at 0.5 km s^{-1}. Most of the absorption comes from the dead zone, where the velocity of the gas is stationary, and an area near the poles, where the line-of-sight velocity is small (see Fig. 3). As a result, the spectrum only shows a small velocity shift. Furthermore, since almost all the absorption comes from gas at low velocities, the width of the spectrum is primarily set by the thermal velocity of the gas.

In Fig. 5, we show how the transit spectrum varies with planetary magnetic field strength. Interestingly, the transit depth does not decrease monotonically with magnetic field strength, even though the fraction of open field lines (and the mass-loss rate) decreases smoothly as a function of magnetic field strength. As the magnetic field strength is increased, the size of the region where the magnetic

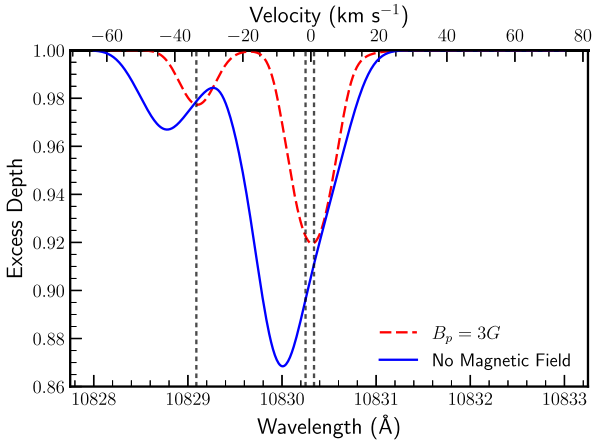


Figure 4. Calculated excess absorption for a planet with (i) no magnetic field (solid blue) and (ii) a surface magnetic field of 3 G (dashed red) at mid-transit with an impact parameter of 0. The velocity scale is centred on the blended transitions at 10 830.25 and 10 830.34 Å.

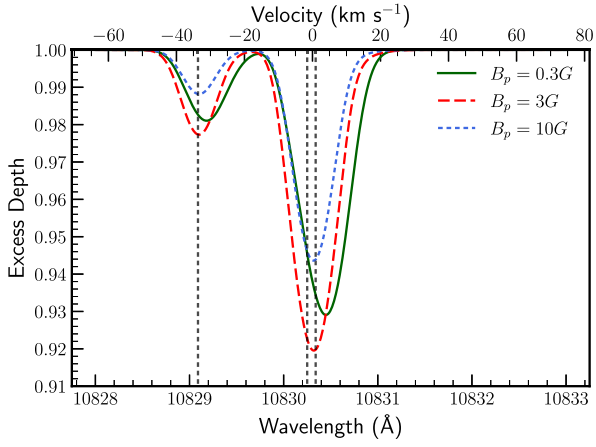


Figure 5. Calculated excess absorption as a function of wavelength for different planetary magnetic field strengths. For a planetary magnetic field of 3 G, we also include a case in which the stellar magnetic field is non-zero. The velocity scale is the same as in Fig. 4.

Downloaded from https://academic.oup.com/mnras/article/527/3/5117/7424142 by Imperial College London Library user on 31 January 2024

field lines are closed increases. This region then blocks more of the stellar disc, contributing more to the transit depth. At the same time, since the mass-loss decreases, the column density of gas in the outflowing regions near the poles decreases, contributing less to the transit depth. The weight of these contributions has an opposite dependence on the strength of the magnetic field and results in the transit depth not being a monotonic function of the magnetic field strength.

The overall velocity shift of the transmission spectrum also varies as the magnetic field strength changes. At lower magnetic field strengths, gas pressure is able to open up field lines at lower latitudes. The gas coupled to these field lines has a higher line-of-sight velocity, resulting in a redshifted spectrum. In the 0.3 G case, shown in Fig. 5, this velocity shift is 3.8 km s^{-1}.

For the 3 G case, we also include a situation where the stellar magnetic field is non-zero, and the ratio of stellar to planetary magnetic field strength is given by $\beta_* = 0.001$. For a planet at 0.04 au around a solar radius star, this corresponds to a stellar surface magnetic field of 1 G. In general, the stellar magnetic field is able to open out more field lines. As mentioned above, this can either increase or decrease the transit depth depending on how the contributions from the closed region and outflowing regions change. However, in this case, we actually see no change in the transit spectrum. This is because the opening of field lines is completely dominated by the outflow rather than the stellar field. This effect is explained in fig. 4 of Owen & Adams (2014).

5 DISCUSSION AND CONCLUSIONS

We have post-processed 2D HD and MHD simulations of a hot Jupiter undergoing photoevaporation and calculated in-transit absorption signal due to the 10 830 Å line of helium. If the planet has no magnetic field, the transit signal is blueshifted $\Delta v = -8.3$ km s^{-1} due to the absorption from gas that flows from the hot dayside to a cold nightside. When a planetary magnetic field (between 0.3 and 10 G) is included, the transit signal has either no apparent velocity shift or a very slight redshift, as escaping gas from the dayside is tied to magnetic field lines and moves away from the observer in transit.

At the current resolution of ground-based instruments, this difference in line-centre velocity is observable and may be used to test whether outflows are magnetically controlled or not and consequently put constraints on the magnetic field strengths of planets. As the observed velocity difference is due to large-scale changes in the geometry of the flow, this method should be fairly robust to the specifics of the photoevaporative flow (e.g. mass-loss rate and temperature). However, further work is required to ensure that our results are still true in full 3D simulations over a more extensive region of parameter space and for various magnetic field configurations. We will discuss this in Section 5.1.1.

For magnetically controlled flows, observationally distinguishing between different planetary magnetic field strengths is a more difficult task. The clearest difference is that lower field strengths with more open field lines lead to a more redshifted transit. More open field lines can also increase high-velocity gas absorption far from the planet, leading to asymmetric transits with an extended red wing. This is only visibly apparent in the 0.3 G case when we consider gas within $8R_p$ instead of $4R_p$ (see Fig. A1 in Appendix A).Observations of the escaping atmosphere of WASP-52b show that the transit spectrum is unshifted with respect to the planet's rest frame and has a slight asymmetry in the red wing. We speculate that this might indicate that the outflow is magnetically controlled. Overall, we caution that since the differences in these spectra are relatively minor, model and observational uncertainties most likely make different magnetic field cases indistinguishable at the resolution of current instruments.

5.1 Limitations

5.1.1 Use of Owen & Adams (2014) simulations and 3D effects

In reality, atmospheric escape is a 3D process, and 3D radiation-MHD simulations that include rotational effects are necessary to confirm the validity of this work. The Owen & Adams (2014) simulations are simplistic when compared to current state-of-the-art simulations; however, as discussed above, they are the only simulation set that included radiative transfer, models with and without magnetic fields, and a reasonable parameter study within the same framework. This allowed us to make meaningful comparisons between simulations that did and did not include magnetic fields. However, it is important to discuss some of the limitations of these simulations so that our results are non-conflated with specific quantitative results arising from our post-processing of this simulation set. The Owen & Adams (2014) simulations were the first multidimensional simulations of photoevaporation that included on-the-fly radiative transfer. As such, they used a simplified algorithm that assumed an ionization–recombination balance for the hydrogen and took the ionized gas to be at 10^4 K, where the temperature was computed based on the local ionization fraction (e.g. Gritschneder et al. 2009). This ionization–recombination balance is well known to be applicable to planets around young stars (e.g. Murray-Clay et al. 2009; Owen & Alvarez 2016), yet most observations of helium outflows are for old planets where this approximation does not hold. The approximations of the Owen & Adams (2014) simulations are likely driving two quantitative results of our simulations: first, the high fluxes produce a high rate of recombinations, and thus, our helium transit depths are likely overestimated compared to older systems; secondly, the outflow velocity (and hence the magnitude of the velocity shift) depends directly of the gas' temperature, with higher temperatures giving higher outflow velocities. Outflows around lower mass, older planets are more likely to be in the 'energy-limited' regime (Owen & Alvarez 2016), where the outflow temperatures are necessarily lower, and hence we suspect that our simulated $\sim$8 km s^{-1} blueshifts are likely overestimates. However, as discussed above, based on the results of more recent 3D simulations, we are confident that our qualitative conclusions about blueshifts arising in the hydrodynamic cases are robust. Hence, the detection or lack of blueshift can be used to make inferences about the strength of any planetary magnetic field.

We also re-emphasize that we focus on a particular area of parameter space where the ram pressure of the planetary wind or the magnetic pressure of the planet dominates over the stellar magnetic pressure or stellar wind ram pressure close to the planet. Whether the stellar wind or stellar magnetic field has a larger influence on the orbit of the planet depends on the mass-loss rate of the star, the magnetic field of the star, stellar wind velocity, and the semimajor axis of the planet. For hot Jupiters, both the case where the stellar magnetic field or the case where stellar wind dominates are possible for sensible stellar and planetary parameters. As the magnetic pressure for a dipolar field drops $\sim r^{-6}$ compared to the stellar wind ram pressure r^{-2}, the stellar wind is more likely to dominate for sub-Neptunes, which are generally further from their star than hot Jupiters.

The primary effect of increasing the strength of the stellar magnetic field is to open more planetary field lines. At low stellar magnetic

Downloaded from https://academic.oup.com/mnras/article/527/3/5117/7424142 by Imperial College London Library user on 31 January 2024

field strengths, this can increase the mass-loss rate. At high stellar magnetic field strengths, the flow cannot smoothly transition through the sonic point along these open field lines, and the mass-loss rate can actually decrease (Owen & Adams 2014). These changes can vary the transit depth. However, we do not expect it to significantly change the velocity of the absorbing gas and therefore the velocity shift of the transit.

On the other hand, the stellar wind may have a significant effect on the velocity shift of the transmission spectrum. If the planet is outside the Alfvén radius of the star, the ram pressure of the stellar wind dominates over the magnetic pressure of the stellar wind and the magnetic field lines in the stellar wind follow the stellar wind plasma.

The effect of the stellar wind on the geometry of the planetary outflow has been studied in both hydrodynamic and MHD simulations. As the strength of the stellar wind is increased compared to the planetary outflow or planetary magnetic field, the stellar wind is able to confine the planetary outflow closer to the surface of the planet. On scales larger than the Hill sphere of the planet, the stellar wind will shape the outflow into a cometary tail that is being radially accelerated away from the star (e.g. Matsakos et al. 2015; Khodachenko et al. 2019; McCann et al. 2019). In essentially isothermal 3D hydrodynamic simulations including helium, MacLeod & Oklopčić (2022) showed that this could result in both blueshifted absorption during the optical transit and significant blueshifted post-optical absorption. This is also apparent in 3D radiation-hydrodynamic simulations performed by Wang & Dai (2021).

MHD simulations, including the radial magnetic field of the stellar wind, have also shown that the stellar wind causes planetary magnetic field lines to bend towards the nightside (e.g. Kislyakova et al. 2014; Carolan et al. 2021b; Khodachenko et al. 2021; Ben-Jaffel et al. 2022). It is possible that this could result in a blueshifted absorption signature during the transit of the planet, even if the planet had a reasonably strong magnetic field. However, it is likely that this would also cause a significant blueshifted post-optical absorption like that seen in the hydrodynamic case. More 3D simulations are necessary to understand how degenerate observations are over the full parameter space.

5.1.2 Eccentricity uncertainty

To definitively assert that the velocity shift is due to the outflow, we must know the planet's eccentricity. Since highly irradiated planets are close to their host stars, they are generally assumed to have undergone orbital circularization. Small deviations away from a circular orbit can cause an apparent velocity shift, $\Delta v_{\rm los}$, of

$$\Delta v_{\rm los} \sim v_k e \cos\omega, \tag{19}$$

where v_k is Keplerian velocity, e is the eccentricity, and ω is the argument of periastron of the planet (e.g. Murray & Correia 2010). Van Eylen et al. (2019) determined the eccentricities for a sample of Kepler planets through a combination of astroseismology and transit light-curve analysis. However, uncertainties in the eccentricity for individual planets were rarely < 0.1. For a planet with a typical orbital velocity of $\sim$100 km s^{-1}, an eccentricity uncertainty of $\sim$0.1 can lead to a velocity shift of $\sim$10 km s^{-1}, which is of the order of the velocity shift due to the outflow geometry. This is also true when transit timing variations (TTVs) are used to determine eccentricities in multiplanetary systems (Van Eylen & Albrecht 2015).

The detection of a secondary eclipse can be used to measure $e\cos\omega$ of individual planets precisely (e.g. Winn 2010), such that we can rule out this as a source of the observed velocity shift. Due to their high temperatures and large size, this is often possible for hot Jupiters (e.g. Charbonneau et al. 2005; Baskin et al. 2013). Previously, this has not generally been the case for sub-Neptunes. However, with *JWST*, detecting the secondary eclipse of some sub-Neptunes might be possible.

5.2 Implications for real systems

Ideally, we would be able to use helium observations to constrain these planets' magnetic fields. As highlighted in the previous section, eccentricity uncertainties generally mean that we cannot make claims about the magnetic field strengths of individual planets based on these observations. However, we speculate about trends in the population.

Table 1 lists spectroscopic detections of helium escape. For each planet, we quote the observed velocity shift of the absorption relative to the planet's rest frame, which is often determined by assuming a circular orbit if the planet is not known to be eccentric. These are not directly comparable to our models, as the observed transit depth is generally computed by integrating over all in-transit phases. We also estimate a critical surface magnetic field strength $B_{\rm c}$ at which the flow transitions from 'hydrodynamic' to 'magnetically controlled' and no longer expect to see a blueshifted transit spectrum. We approximate this value as the maximum surface magnetic field so that the outflow opens all field lines. Although, we caution that this is likely to be an overestimate. Since the outflow may be able to wrap around to the nightside in the terminator region before all field lines are opened, 3D MHD simulations will be required to investigate this quantitatively.

This critical magnetic field strength is found by requiring that the thermal pressure exceeds the magnetic pressure for $r > R_{\rm p}$. We estimate the thermal pressure by (i) assuming that the outflow is an isothermal Parker wind with a fixed sound speed and mass-loss rate or (ii) assuming that the outflow is in photoionization equilibrium. In both cases, the detailed procedure used to calculate the critical magnetic field is explained in Appendix B. In Table 1, we give three critical magnetic field strength values. The first two are calculated assuming the isothermal Parker wind case, where the sound speed is 0.3×10^4 K/10^4 K, and the mass-loss rate is given by the energy-limited mass-loss rate (equation 2) with efficiency $\eta = 0.1$. The final estimate is given by the photoionization equilibrium case, where the gas temperature is 10^4 K. In general, this last method gives a slightly larger value for the critical magnetic field but is the least applicable to old planets.

To calculate the critical magnetic field strength, we needed to estimate the $F_{\rm uv}$ received by each planet. For this, we used values given in each of the cited detection papers (see Table 1). If no estimate was present, we used estimates from Kirk et al. (2022) in which they found the combined X-ray and UV (XUV) flux by comparing to stars of similar spectra from the MUSCLES survey (France et al. 2016; Loyd et al. 2016; Youngblood et al. 2016). We note that the reconstructed XUV flux has significant uncertainties, and our methods for calculating the thermal pressure of the outflow are only approximate. Therefore, we expect that our estimates for $B_{\rm c}$ may vary by an order of magnitude.

We also estimate the extent to which the stellar wind can confine the outflow. To effectively radially accelerate the planetary gas to produce a blueshifted transit, the stellar wind must be able to penetrate close to the planetary surface. We approximately calculate the position of the bow shock produced when the stellar wind and planetary outflow collide. The bow shock is defined by the condition that the momentum fluxes of the stellar wind and planetary outflow balance. In the simple case, where outflows are spherical, we can

Downloaded from https://academic.oup.com/mnras/article/527/3/5117/7424142 by Imperial College London Library user on 31 January 2024

Table 1. Detections of helium atmospheric escape using high-resolution spectroscopy and the observed velocity shift of the outflow in the rest frame of the planet. We have provided uncertainties on the observed velocity shift, where given in the detection paper. These are generally of the order of a few km s^{-1}. We estimate the maximum surface magnetic field B_c such that all field lines are opened by the planetary outflow. The three numbers correspond to estimating strengths when we approximate the outflow to be (i) an isothermal Parker wind at 10^4 K, (ii) an isothermal Parker wind at 0.3×10^4 K, and (iii) in photoionization–recombination equilibrium. For the former two calculations, we estimate the mass-loss rate of the planet using the energy-limited formula with an efficiency of 0.1. We also estimate the bow shock radii at which the stellar wind collides with the planetary outflow (equation 20) and the magnetosphere corresponding to a planet with a surface magnetic field of 1 G (equation 21). The minimum absorption area is a lower limit on the extent of the outflow assuming that it is optically thick.

Planet name	Radius (R_J)	B_c (G)	Bow shock radius – hydrodynamic (R_p)	Bow shock radius – magnetic (R_p)	Observed velocity shift (km s^{-1})	Minimum absorber area (R_p)	Reference
GJ 1214b	0.24	0.003 0.005 0.15	0.2	7.1	-5^{+4}_{-7}	1.6	Orell-Miquel et al. (2022)[a]
GJ 3470b	0.36	0.01 0.02 0.24	1.2	10.5	-3.2 ± 1.3	1.9	Palle et al. (2020)
Hat-P−11b	0.39	0.01 0.05 0.30	1.7	13.5	-3	2.2	Allart et al. (2018)
HD 189733b	1.13	0.19 1.56 0.54	1.1	10.3	-3.5 ± 0.4	1.2	Salz et al. (2018)
HD 209458b	1.39	0.02 0.15 0.23	0.7	12.9	-1.8 ± 1.3	1.3	Alonso-Floriano et al. (2019)
TOI-1430.01	0.18	0.02 0.05 0.45	5.4	15.7	-4.0 ± 1.3	3.6	Zhang et al. (2023)
TOI-1683.01	0.18	0.03 0.08 0.53	3.4	11.3	-6.7 ± 2.8	3.4	Zhang et al. (2023)
TOI-2076b	0.22	0.03 0.06 0.46	5.7	14.9	-6.7 ± 1.4	3.5	Zhang et al. (2023)[b]
TOI-560b	0.25	0.02 0.04 0.38	3.8	14.6	4.3 ± 1.4	2.4	Zhang et al. (2022)
WASP-107b	0.92	0.01 0.03 0.23	2.5	13.9	-2.4 ± 0.4	2.2	Kirk et al. (2020)
WASP-52b	1.2	0.06 0.43 0.49	2.2	9.6	0.0 ± 1.2	1.6	Kirk et al. (2022)
WASP-69b	1.0	0.02 0.13 0.32	2.0	12.6	-3.6 ± 0.2	1.8	Nortmann et al. (2018)

[a]Subsequent observations by Kasper et al. (2020) and Spake et al. (2022) have failed to detect escaping helium.
[b]Gaidos et al. (2023) also observed this planet but attributed the detection to stellar activity.

approximate the radial distance of the bow shock from the planet r_b:

$$r_b = a\sqrt{\frac{\dot{M}c_s}{\dot{M}_* u_*}}, \tag{20}$$

where $\dot{M}_*$ is the mass-loss rate of the star, $\dot{M}$ is the mass-loss rate of the planet, u_* is the stellar wind velocity, and a is the semimajor axis of the planet. To calculate r_b, we estimate the mass-loss rate of the planet using the energy-limited mass-loss rate (equation 2) with efficiency $\eta = 0.1$ and use solar-like wind values of $\dot{M}_* = 10^{-14}\,M_\odot\,\mathrm{yr}^{-1}$ and $u_* = 150$ km s^{-1}. If significant absorption occurs outside this radius, then the stellar wind is likely to play an important role in determining the shape of the transit. We also note that a strong planetary magnetic field can considerably increase the bow shock distance. In this case, the bow shock distance is approximated by the point at which the stellar wind ram pressure and magnetic pressure of the planetary field balance. Therefore, we also calculate the position of the bow shock considering the effects of a 1 G surface magnetic field. Here, the expression for r_b is given by

$$r_b = \left(\frac{B_0^2 a^2}{2\dot{M}_* u_*}\right)^{\frac{1}{4}}. \tag{21}$$

Interestingly, 10 out of the 12 systems show blueshifted absorption. Thus, it is highly unlikely that uncertainties in planetary motion can account for all of these. Therefore, it is likely that some of these blueshifts can be attributed to the geometry of the outflow. There are two explanations for this. The first possibility is that these planets have relatively weak surface magnetic fields ($B \lesssim 0.1$ G), and day-

Downloaded from https://academic.oup.com/mnras/article/527/3/5117/7424142 by Imperial College London Library user on 31 January 2024

to-night winds are responsible for the blueshifted transit. For sub-Neptunes, this would agree with the findings of Owen (2019), which demonstrated that the suppression of atmospheric mass-loss by the presence of surface magnetic fields $\gtrsim$0.3 G is not consistent with both the position of the radius valley and the rocky composition of planets below the valley. This is not inconsistent with dynamo-generated magnetic fields in the cores of sub-Neptunes being of the order of a few Gauss, like Solar system planets, as a few per cent by mass hydrogen/helium envelope can greatly increase the radius of the planet and particularly raise the upper atmosphere where atmospheric mass-loss is taking place. Since magnetic field strength for a dipole field scales like r^{-3}, the magnetic field can be much weaker in these regions. For hot Jupiters, this conclusion would favour the argument of Grießmeier et al. (2004) that slow rotation of hot Jupiters due to tidal locking leads to magnetic fields that are orders of magnitude smaller than Jupiters. This is in opposition to the argument of Christensen et al. (2009), which predicts magnetic field strengths an order of magnitude greater than Jupiters, based on a scaling relation between magnetic field strength and energy flux.

The other possibility is that stellar winds are able to penetrate close to the planetary surface and radially accelerate the gas to produce the observed blueshifts. We note that a comet-like tail of escaping helium extending out to $\sim$7 planetary radii has been detected in the case WASP-107b (Spake, Oklopčić & Hillenbrand 2021) and to a lesser extent for WASP-69b (Nortmann et al. 2018), HAT-P-18b (Fu et al. 2022), and HD 189733b (Guilluy et al. 2020). This may be evidence that the stellar wind plays a role in shaping the outflow of some of these planets. We can set a lower limit on the extent of the outflow by assuming that the gas is optically thick to 10 830 Å radiation, which can be compared to the bow shock radius to assess the importance of stellar wind. We call this the 'minimum absorption area', and calculate its value at mid-transit (see Table 1). We stress that the gas is optically thin (e.g. MacLeod & Oklopčić 2022) and therefore the actual extent can be significantly larger than this estimate. A good example of this is the transit of WASP-107b, which is found to a have a much smaller minimum absorption area $\sim 2R_{\rm p}$, than is temporally observed $\sim 7R_{\rm p}$ (e.g. Spake et al. 2022).

In general, if the planets have weak magnetic fields, solar or moderately supersolar winds are required to set the bow shock radius close enough to the planet to disrupt the planetary outflow significantly. This is certainly feasible based on estimates of stellar wind mass rates from detections of astrospheric absorption (e.g. Wood et al. 2005, 2021). However, if these planets are able to host significant surface magnetic fields ($B \gtrsim 1$ G), then stellar winds with mass-loss rates orders of magnitude greater than the Sun would be required. Thus, we speculate that regarding the population of close-in planets for which helium observations have been taken, there is no evidence that these planets possess magnetic field strengths strong enough to control the topology of any photoevaporative outflow.

ACKNOWLEDGEMENTS

We thank the anonymous reviewer for their comments, which improved the manuscript. We are grateful to James Kirk for useful discussions. JEO was supported by a Royal Society University Research Fellowship. This project has received funding from the European Research Council (ERC) under the European Union's Horizon 2020 research and innovation programme (Grant agreement No. 853022, PEVAP). For the purpose of open access, the authors have applied a Creative Commons Attribution (CC-BY) licence to any Author Accepted Manuscript version arising.

DATA AVAILABILITY

The data underlying this article will be shared on reasonable request to the authors.

REFERENCES

Adams F. C., 2011, ApJ, 730, 27
Allart R. et al., 2018, Science, 362, 1384
Alonso-Floriano F. J. et al., 2019, A&A, 629, A110
Arakcheev A. S., Zhilkin A. G., Kaigorodov P. V., Bisikalo D. V., Kosovichev A. G., 2017, Astron. Rep., 61, 932
Arras P., Socrates A., 2010, ApJ, 714, 1
Baraffe I., Selsis F., Chabrier G., Barman T. S., Allard F., Hauschildt P. H., Lammer H., 2004, A&A, 419, L13
Baskin N. J. et al., 2013, ApJ, 773, 124
Batygin K., Stevenson D. J., 2010, ApJ, 714, L238
Batygin K., Stevenson D. J., Bodenheimer P. H., 2011, ApJ, 738, 1
Ben-Jaffel L. et al., 2022, Nat. Astron., 6, 141
Bodenheimer P., Lin D. N. C., Mardling R. A., 2001, ApJ, 548, 466
Bray I., Burgess A., Fursa D. V., Tully J. A., 2000, A&AS, 146, 481
Brown R. L., 1971, ApJ, 164, 387
Carolan S., Vidotto A. A., Villarreal D'Angelo C., Hazra G., 2021a, MNRAS, 500, 3382
Carolan S., Vidotto A. A., Hazra G., Villarreal D'Angelo C., Kubyshkina D., 2021b, MNRAS, 508, 6001
Carroll-Nellenback J., Frank A., Liu B., Quillen A. C., Blackman E. G., Dobbs-Dixon I., 2016, MNRAS, 466, 2458
Cauley P. W., Shkolnik E. L., Llama J., Lanza A. F., 2019, Nat. Astron., 3, 1128
Charbonneau D. et al., 2005, ApJ, 626, 523
Christensen U. R., Holzwarth V., Reiners A., 2009, Nature, 457, 167
Connerney J. E. P. et al., 2022, J. Geophys. Res. (Planets), 127, e07055
Cranmer S. R., 2004, Am. J. Phys., 72, 1397
Debrecht A., Carroll-Nellenback J., Frank A., Blackman E. G., Fossati L., McCann J., Murray-Clay R., 2020, MNRAS, 493, 1292
Dorn C., Harrison J. H. D., Bonsor A., Hands T. O., 2018, MNRAS, 484, 712
Drake G. W., 1971, Phys. Rev. A, 3, 908
Dressing C. D. et al., 2015, ApJ, 800, 135
France K. et al., 2016, ApJ, 820, 89
Fu G. et al., 2022, ApJ, 940, L35
Fulton B. J. et al., 2017, AJ, 154, 109
Gaidos E. et al., 2023, MNRAS, 518, 3777
Ginzburg S., Sari R., 2016, ApJ, 819, 116
Ginzburg S., Schlichting H. E., Sari R., 2018, MNRAS, 476, 759
Grießmeier J. M. et al., 2004, A&A, 425, 753
Gritschneder M., Naab T., Walch S., Burkert A., Heitsch F., 2009, ApJ, 694, L26
Guillot T., Showman A. P., 2002, A&A, 385, 156
Guilluy G. et al., 2020, A&A, 639, A49
Gupta A., Schlichting H. E., 2019, MNRAS, 487, 24
Hubbard W. B., Hattori M. F., Burrows A., Hubeny I., Sudarsky D., 2007, Icarus, 187, 358
Hummer D. G., Storey P. J., 1998, MNRAS, 297, 1073
Jackson A. P., Davis T. A., Wheatley P. J., 2012, MNRAS, 422, 2024
Jin S., Mordasini C., Parmentier V., van Boekel R., Henning T., Ji J., 2014, ApJ, 795, 65
Kasper D., Bean J. L., Oklopčić A., Malsky I., Kempton E. M. R., Désert J.-M., Rogers L. A., Mansfield M., 2020, AJ, 160, 258
Khodachenko M. L., Shaikhislamov I. F., Fossati L., Lammer H., Rumenskikh M. S., Berezutsky A. G., Miroshnichenko I. B., Efimof M. A., 2021, MNRAS, 503, L23

Downloaded from https://academic.oup.com/mnras/article/527/3/5117/7424142 by Imperial College London Library user on 31 January 2024

Khodachenko M. L., Shaikhislamov I. F., Lammer H., Berezutsky A. G., Miroshnichenko I. B., Rumenskikh M. S., Kislyakova K. G., Dwivedi N. K., 2019, ApJ, 885, 67
Khodachenko M. L., Shaikhislamov I. F., Lammer H., Prokopov P. A., 2015, ApJ, 813, 50
Kirk J., Alam M. K., López-Morales M., Zeng L., 2020, AJ, 159, 115
Kirk J., Dos Santos L. A., López-Morales M., Alam M. K., Oklopčić A., MacLeod M., Zeng L., Zhou G., 2022, AJ, 164, 24
Kislyakova K. G., Holmström M., Lammer H., Odert P., Khodachenko M. L., 2014, Science, 346, 981
Komacek T. D., Youdin A. N., 2017, ApJ, 844, 94
Kramida A., Ralchenko Y., Reader J., NIST ASD Team, 2022, NIST Atomic Spectra Database (ver. 5.10), [Online]. Available: https://physics.nist.gov/asd(accessed 2017 April 9). National Institute of Standards and Technology, Gaithersburg, MD
Kubyshkina D. et al., 2018, A&A, 619, A151
Kulow J. R., France K., Linsky J., Loyd R. O. P., 2014, ApJ, 786, 132
Lammer H., Selsis F., Ribas I., Guinan E. F., Bauer S. J., Weiss W. W., 2003, ApJ, 598, L121
Landsman W., Simon T., 1993, ApJ, 408, 305
Laughlin G., Crismani M., Adams F. C., 2011, ApJ, 729, L7
Lecavelier Des Etangs A. et al., 2010, A&A, 514, A72
Lee E. J., Connors N. J., 2021, ApJ, 908, 32
Lee E. J., Karalis A., Thorngren D. P., 2022, ApJ, 941, 186
Lopez E. D., Fortney J. J., 2013, ApJ, 776, 2
Loyd R. O. P. et al., 2016, ApJ, 824, 102
Lundkvist M. S. et al., 2016, Nat. Commun., 7, 11201
Luque R., Pallé E., 2022, Science, 377, 1211
MacLeod M., Oklopčić A., 2022, ApJ, 926, 226
Malsky I., Rogers L. A., 2020, ApJ, 896, 48
Martin W. C., 1973, J. Phys. Chem. Ref. Data, 2, 257
Matsakos T., Uribe A., Königl A., 2015, A&A, 578, A6
McCann J., Murray-Clay R. A., Kratter K., Krumholz M. R., 2019, ApJ, 873, 89
Menou K., 2012, ApJ, 745, 138
Muñoz A., 2007, Planet. Space Sci., 55, 1426
Murray C. D., Correia A. C. M., 2010, in Seager S., ed., Exoplanets. University of Arizona Press, Tucson, AZ, p. 15
Murray-Clay R. A., Chiang E. I., Murray N., 2009, ApJ, 693, 23
Nortmann L. et al., 2018, Science, 362, 1388
Oklopčić A., 2019, ApJ, 881, 133
Oklopčić A., Hirata C. M., 2018, ApJ, 855, L11
Oklopčić A., Silva M., Montero-Camacho P., Hirata C. M., 2020, ApJ, 890, 88
Orell-Miquel J. et al., 2022, A&A, 659, A55
Osterbrock D. E., Ferland G. J., 2006, in Astrophysics of Gaseous Nebulae and Active Galactic Nuclei, 2nd edn. University Science Books, Mill Valley, CA
Owen J. E. et al., 2023, MNRAS, 518, 4357
Owen J. E., 2019, Annu. Rev. Earth Planet. Sci., 47, 67
Owen J. E., Adams F. C., 2014, MNRAS, 444, 3761
Owen J. E., Adams F. C., 2019, MNRAS, 490, 15
Owen J. E., Alvarez M. A., 2016, ApJ, 816, 34
Owen J. E., Jackson A. P., 2012, MNRAS, 425, 2931
Owen J. E., Lai D., 2018, MNRAS, 479, 5012
Owen J. E., Wu Y., 2013, ApJ, 775, 105
Owen J. E., Wu Y., 2017, ApJ, 847, 29
Palle E. et al., 2020, A&A, 638, A61
Perna R., Menou K., Rauscher E., 2010, ApJ, 724, 313
Petzold L., 1983, SIAM J. Sci. Stat. Comput., 4, 136
Rauscher E., Menou K., 2013, ApJ, 764, 103
Roberge W., Dalgarno A., 1982, ApJ, 255, 489
Rogers J. G., Janó Muñoz C., Owen J. E., Makinen T. L., 2023b, MNRAS, 519, 6028
Rogers J. G., Owen J. E., 2021, MNRAS, 503, 1526
Rogers J. G., Schlichting H. E., Owen J. E., 2023, ApJL, 947,L19
Salz M. et al., 2018, A&A, 620, A97
Spake J. J. et al., 2018, Nature, 557, 68
Spake J. J. et al., 2022, ApJ, 939, L11
Spake J. J., Oklopčić A., Hillenbrand L. A., 2021, AJ, 162, 284
Stevenson D. J., 2003, Earth Planet. Sci. Lett., 208, 1
Stone J. M., Proga D., 2009, ApJ, 694, 205
Szabó G. M., Kiss L. L., 2011, ApJ, 727, L44
Thorngren D. P., Fortney J. J., 2018, AJ, 155, 214
Trammell G. B., Arras P., Li Z.-Y., 2011, ApJ, 728, 152
Trammell G. B., Li Z.-Y., Arras P., 2014, ApJ, 788, 161
Tripathi A., Kratter K. M., Murray-Clay R. A., Krumholz M. R., 2015, ApJ, 808, 173
Van Eylen V. et al., 2019, AJ, 157, 61
Van Eylen V., Agentoft C., Lundkvist M. S., Kjeldsen H., Owen J. E., Fulton B. J., Petigura E., Snellen I., 2018, MNRAS, 479, 4786
Van Eylen V., Albrecht S., 2015, ApJ, 808, 126
Vidal-Madjar A., Lecavelier des Etangs A., Désert J. M., Ballester G. E., Ferlet R., Hébrard G., Mayor M., 2003, Nature, 422, 143
Virtanen P. et al., 2020, Nat. Methods, 17, 261
Wang L., Dai F., 2021, ApJ, 914, 99
Winn J. N., 2010, in Seager S., ed., Exoplanets. University of Arizona Press, Tucson, AZ, p. 55
Wood B. E. et al., 2021, ApJ, 915, 37
Wood B. E., Redfield S., Linsky J. L., Müller H.-R., Zank G. P., 2005, ApJS, 159, 118
Wu Y., 2019, ApJ, 874, 91
Wyatt M. C., Kral Q., Sinclair C. A., 2020, MNRAS, 491, 782
Youdin A. N., Mitchell J. L., 2010, ApJ, 721, 1113
Youngblood A. et al., 2016, ApJ, 824, 101
Zeng L. et al., 2019, Proc. Natl. Acad. Sci. USA, 116, 9723
Zhang M., Knutson H. A., Dai F., Wang L., Ricker G. R., Schwarz R. P., Mann C., Collins K., 2023, AJ, 165, 62
Zhang M., Knutson H. A., Wang L., Dai F., Barragán O., 2022, AJ, 163, 67

APPENDIX A: ADDITIONAL TRANSIT PROFILES

Transit spectra when gas within $8R_p$ is taken into account rather than $4R_p$ are shown in Fig. A1. They are qualitatively similar to our standard case.

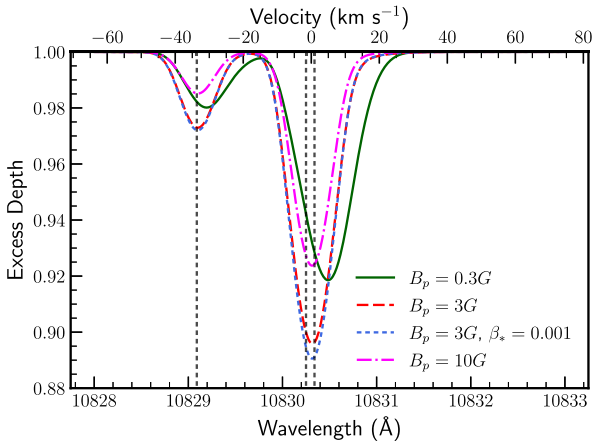


Figure A1. Calculated excess absorption as a function of wavelength for different planetary magnetic field strengths where we took into account gas within $8R_p$ of the planet. The 0.3 G case now has an extended red wing due to absorption of high-velocity gas far from the star.

Downloaded from https://academic.oup.com/mnras/article/527/3/5117/7424142 by Imperial College London Library user on 31 January 2024

APPENDIX B: SOLVING FOR THE CRITICAL MAGNETIC FIELD STRENGTH

B1 Assuming that the outflow is an isothermal Parker wind

Here, we outline the procedure to obtain the critical magnetic field strength when we approximate the outflow to be an isothermal Parker wind. For a given mass-loss rate and sound speed, the density and gas pressure can be written analytically in terms of the Lambert W function (Cranmer 2004). The magnetic pressure along this streamline is given by

$$P_B = \frac{B_0^2}{8\pi}\left(\frac{R_\mathrm{p}}{r}\right)^6. \tag{B1}$$

The critical magnetic field is given by the value of the surface magnetic field such that gas pressure exceeds the magnetic pressure over for $r > R_\mathrm{p}$ except one point where they are equal, which denotes r_B. Either this point is R_p or at this point the magnetic pressure and thermal pressure are tangent. If they are tangent at this point, the thermal and magnetic pressure should satisfy

$$P_\mathrm{th}(r_B) = P_B(r_B), \tag{B2}$$

$$\frac{\mathrm{d}P_\mathrm{th}}{\mathrm{d}r}(r_B) = \frac{\mathrm{d}P_B}{\mathrm{d}r}(r_B). \tag{B3}$$

We can combine these two equations by inserting the form of the magnetic pressure (equation B1) in order to get an equation just in terms of the thermal pressure:

$$\frac{\mathrm{d}P_\mathrm{th}}{\mathrm{d}r}(r) + \frac{6P_\mathrm{th}(r)}{r} = 0. \tag{B4}$$

Using the Lambert W function (Cranmer 2004), the thermal pressure is given by

$$P_\mathrm{th}(r) = \frac{\dot{M}c_\mathrm{s}^2}{4\pi r^2 u(r)}, \tag{B5}$$

$$u = \begin{cases} -c_\mathrm{s}^2 W_0[-D(r)] & r \le r_\mathrm{c}, \\ -c_\mathrm{s}^2 W_{-1}[-D(r)] & r > r_\mathrm{c}, \end{cases} \tag{B6}$$

$$D(r) = \left(\frac{r}{r_\mathrm{c}}\right)^{-4} \exp\left[4\left(1 - \frac{r_\mathrm{c}}{r}\right) - 1\right], \tag{B7}$$

and the derivative of the thermal pressure is given by

$$\frac{\mathrm{d}P}{\mathrm{d}r} = -\frac{\dot{M}c_\mathrm{s}^2(2ru(r) + r^2\frac{\mathrm{d}u}{\mathrm{d}r})}{4\pi r^4 u(r)^2}, \tag{B8}$$

$$\frac{\mathrm{d}u}{\mathrm{d}r} = \begin{cases} c_\mathrm{s}\dfrac{\sqrt{-W_0[-D(r)]}}{2D(r)(W_0[-D(r)]+1)} & r \le r_\mathrm{c}, \\ c_\mathrm{s}\dfrac{\sqrt{-W_{-1}[-D(r)]}}{2D(r)(W_{-1}[-D(r)]+1)} & r \ge r_\mathrm{c}. \end{cases} \tag{B9}$$

Equation (B4) can be numerically solved for r_B. If $r_B > R_\mathrm{p}$, the conditions of equation (B2) are satisfied and the critical magnetic field strength is given by

$$B_\mathrm{c} = \sqrt{\frac{2\dot{M}c_\mathrm{s}^2}{r_B^2 u(r_B)}\left(\frac{r_B}{R_\mathrm{p}}\right)^6}. \tag{B10}$$

An example of this case is shown in the left-hand panel of Fig. B1 (corresponding to HD 189733b). If $r_B < R_\mathrm{p}$, there does not exist a magnetic field strength in which the conditions of equation (B2) are satisfied. Therefore, we set the critical magnetic field strength to be such that the magnetic pressure equals gas pressure at R_p, which is equivalent to setting $P_\mathrm{th}(R_\mathrm{p}) = P_B(R_\mathrm{p})$. Therefore, B_c is given by

$$B_\mathrm{c} = \sqrt{\frac{2\dot{M}c_\mathrm{s}^2}{R_\mathrm{p}^2 u(R_\mathrm{p})}}. \tag{B11}$$

An example of this case is shown in the right-hand panel of Fig. B1 (corresponding to WASP-107b).

B2 Assuming that the outflow is in photoionization equilibrium

For completeness, we also estimate this critical transition assuming that the flow is in photoionization equilibrium (e.g. Owen & Adams 2014; Owen & Alvarez 2016). We note that this is not the case for old low-mass planets. In this case, we approximate that all field lines are opened if the pressure at the base of the flow is greater than the magnetic pressure. We denote this ratio as κ:

$$\kappa = \frac{B_0^2}{8\pi P_0}, \tag{B12}$$

where P_0 is the surface pressure. The surface pressure is calculated by balancing the number of incoming photons with the number of recombinations at the ionization front, assuming that the ionization front is located deep in the planet's atmosphere. Using equation (50) from Owen & Adams (2014) as our starting point, the surface pressure can be cast in terms of the planetary properties and the incident flux:

$$P_0 \approx 5 \times 10^{-13}\sqrt{\frac{GM_\mathrm{p}c_\mathrm{s}^2 F_\mathrm{uv}}{R_\mathrm{p}^2}}\ \mathrm{dyn}, \tag{B13}$$

where F_uv is the incident UV flux. Therefore, the critical magnetic field strength becomes

$$B_\mathrm{c} \approx 0.25\left(\frac{M_\mathrm{p}}{M_\mathrm{J}}\right)^{\frac{1}{4}}\left(\frac{F_\mathrm{uv}}{10^4\ \mathrm{erg\ s^{-1}}}\right)^{\frac{1}{4}}\left(\frac{c_\mathrm{s}}{10\ \mathrm{km\ s^{-1}}}\right)^{\frac{1}{2}}\left(\frac{R_\mathrm{p}}{R_\mathrm{J}}\right)^{-\frac{1}{2}}. \tag{B14}$$

Downloaded from https://academic.oup.com/mnras/article/527/3/5117/7424142 by Imperial College London Library user on 31 January 2024

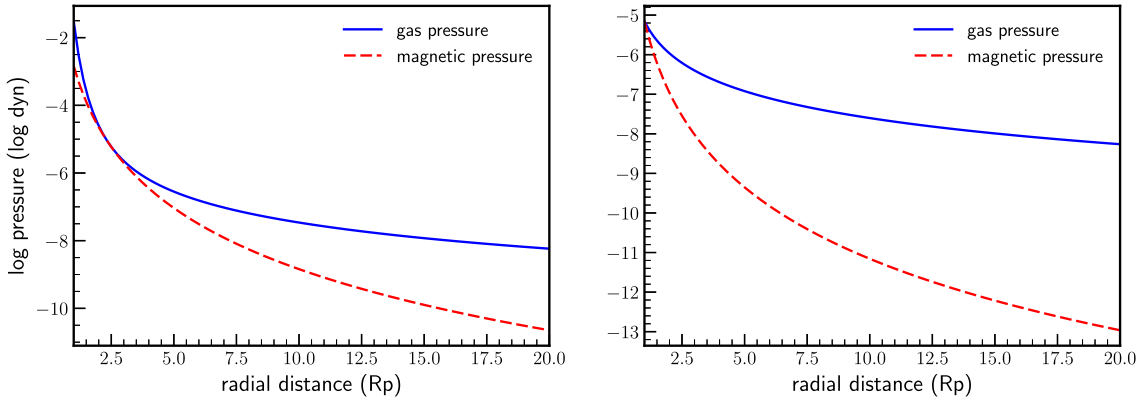


Figure B1. A comparison between the magnetic pressure and gas pressure at the critical magnetic field strength for HD 189733b (left) and WASP-107b (right) assuming that the outflow is an isothermal Parker wind at 10^4 K.

This paper has been typeset from a TEX/LATEX file prepared by the author.

Downloaded from https://academic.oup.com/mnras/article/527/3/5117/7424142 by Imperial College London Library user on 31 January 2024

© 2023 The Author(s).
Published by Oxford University Press on behalf of Royal Astronomical Society. This is an Open Access article distributed under the terms of the Creative Commons Attribution License (https://creativecommons.org/licenses/by/4.0/), which permits unrestricted reuse, distribution, and reproduction in any medium, provided the original work is properly cited